



## Full length article

## Enhanced radiation tolerance of the Ni-Co-Cr-Fe high-entropy alloy as revealed from primary damage

Yeping Lin<sup>a</sup>, Tengfei Yang<sup>a</sup>, Lin Lang<sup>a</sup>, Chang Shan<sup>a</sup>, Huiqiu Deng<sup>b,\*</sup>, Wangyu Hu<sup>a</sup>, Fei Gao<sup>c,\*</sup><sup>a</sup> College of Materials Science and Engineering, Hunan University, Changsha 410082, China<sup>b</sup> School of Physics and Electronics, Hunan University, Changsha 410082, China<sup>c</sup> Department of Nuclear Engineering and Radiological Sciences, University of Michigan, Ann Arbor, MI 48109, USA

## ARTICLE INFO

## Article history:

Received 5 February 2020

Revised 16 June 2020

Accepted 17 June 2020

Available online 23 June 2020

## Keywords:

High entropy alloys

Displacement cascade

Radiation resistance

Interstitial dislocation loop

Molecular dynamics

## ABSTRACT

High-entropy alloys (HEAs) have received much attention for the development of nuclear materials because of their excellent irradiation tolerance. In the present study, the generation and evolution of irradiation-induced defects in the NiCoCrFe HEA were investigated by molecular dynamics (MD) simulations to understand the mechanisms of its irradiation tolerance compared with bulk Ni. The displacement cascades were simulated for the energies of primary knock-on atoms (PKA) ranging from 10 to 50 keV to understand the irradiation resistance in HEAs. In general, there are more displaced atoms produced in the thermal spike phase, but fewer defects survived at the end of the cascades in the NiCoCrFe alloy than in Ni. Both interstitial and vacancy clusters increase in size or number with increasing PKA energy in both materials, but they do so more slowly in the NiCoCrFe HEA. The delayed damage accumulations in the NiCoCrFe HEA are attributed to the high defect recombination caused by the following two mechanisms. First, the enhanced thermal spike and the low thermal conductivity of HEAs for heat dissipation result in the higher efficiency of defect recombination. Furthermore, the substantially small binding energies of interstitial loops in the NiCoCrFe HEA, as compared with those in Ni, are responsible for the delayed interstitial clustering in the NiCoCrFe HEA.

© 2020 Acta Materialia Inc. Published by Elsevier Ltd. All rights reserved.

## 1. Introduction

High-entropy alloys (HEAs) have drawn significant attention for their outstanding material properties, such as high yield strength [1–4], fracture toughness [5,6], wear resistance [7,8], and corrosion resistance [9,10]. They consist of at least four to five principle elements in equal or nearly equal concentrations in a single-phase structure [11–13], which is quite different from conventional alloys. Recently, HEAs have been considered to be promising structural materials for fusion and generation IV fission reactors to address the increasing demands for nuclear energy [14,15].

It is well established that materials, upon irradiation, exhibit hardening and swelling that can result in a sharp degradation of performance [16,17]. A general way to enhance irradiation tolerance is to introduce high-density defect sinks in materials, which has been demonstrated in many conventional alloys, including oxide-dispersion-strengthened steels [18,19], nanolayered [20] and nanograin polycrystalline alloys [21]. However, these structures

are often unstable at high temperatures and in extreme radiation environments [22]. HEAs, especially Ni-based HEAs [23–26]–[27], not only exhibit high-temperature strength [28] and good microstructural stability [29,30] but also present a novel way to reduce irradiation-induced structural damage by only tuning their alloy compositions without preexisting defect sinks [31]. These compositional effects grant Ni-based HEAs potentially improved irradiation resistance according to recent experiments and simulations. From experiments, it is found that the swelling resistance of Ni-based HEAs can be effectively enhanced by modifying the alloy composition [32]. The multichemical species, in Ni-based HEAs, are reported to be able to reduce the mean free path of electrons, phonons and magnons; this modification can affect energy dissipation and, consequently, the defect evolution at very early stages [33–37]. Additionally, the suppressed defect accumulation has also been observed in NiCoCr [27] and NiCoCrFeMn HEAs [38] by simulations.

However, the irradiation-tolerance mechanisms of Ni-based HEAs are still in debate and remain unexplored due to their complex irradiation responses and multiatomic interactions. For example, it is well known that higher densities of small defects

\* Corresponding authors.

E-mail addresses: [hqdeng@hnu.edu.cn](mailto:hqdeng@hnu.edu.cn) (H. Deng), [gaofei@umich.edu](mailto:gaofei@umich.edu) (F. Gao).

have been observed in the HEAs, when compared with those of pure metals, in experiments [15,22]. Recently, some investigations [11,25,27,38,39] have shown that the defect production at a low dose for Ni is approaching that of Ni-based alloys. Furthermore, when compared to pure Ni, other HEAs, such as NiFe and NiCoFe, produce more defects at a low dose [27]. However, with increasing irradiation dose, the defect accumulation in pure Ni continues to increase without saturation, whereas Ni-based HEAs exhibit saturation at a relatively low dose [11,25,39]. This observation suggests that the underlying mechanisms behind the enhanced irradiation resistance of HEAs may not play an important role at low dose, but may be important with increasing dose. More detailed studies are needed to reveal the fundamental mechanisms.

The generation, distribution and evolution of defects in the early stage of displacement cascades are important information for obtaining the mechanisms of irradiation resistance, which has been examined by many researchers [17,26,27,40–42]. For example, the separation between vacancy and interstitial clusters has been observed in Ni-based HEAs and is considered to play an important role in resisting void swelling [22]. The formation of dislocation loops is the main contributors for irradiation induced hardening of FeNiMnCr HEA at room temperature and higher temperature irradiations [29]. Moreover, the lattice defects in the CuNiCoFe HEA that were generated by irradiation have been shown to act as sinks for Cu segregation [11]. However, the researches regarding primary irradiation-induced defects in Ni-based HEAs are rare, and fundamental studies about dislocation loops or voids [43,44] are also lacking, which is due to the difficulty in the accurately analyzing the atomic-level defect generation and evolution mechanisms through experimental techniques alone. The molecular dynamics (MD) method can be employed to simulate the displacement cascade process, defect migration behavior and defect interactions at the atomic scale, which is very useful to reveal the mechanisms for irradiation resistance of HEAs. The NiCoCrFe HEA has recently obtained considerable attention [24,34,45,46–47] and is an ideal model alloy system for further investigations. However, the formation of large defect clusters in the NiCoCrFe HEA has not been observed in MD simulations, which may be due to its ultrahigh defect inhibition and the limited timescale [22,48].

In this research, using MD simulations, we performed a series of displacement cascade simulations in NiCoCrFe HEA and Ni with different PKA energies ( $E_{\text{PKA}}$ ) at the same temperature. We elucidated the mechanisms of defect generation and evolution, including point defects, defect clusters and dislocation loops in the NiCoCrFe HEA and compared the results to those of pure Ni. It is of interest to note that point defect accumulation is delayed in the NiCoCrFe HEA compared to in pure Ni. Additionally, there is a slower clustering of interstitials and the inhibited growth of vacancy clusters in the NiCoCrFe HEA, which is in good agreement with the experimental observations by Lu et al. [15,22]. The present study of defect generation and evolution in NiCoCrFe HEA presents a fundamental understanding of the irradiation-resistance mechanisms in NiCoCrFe, which may also be applied to other HEAs.

## 2. Methodology

### 2.1. Model and simulation

The MD simulations of the displacement cascades were performed using the Large-scale Atomic/Molecular Massively Parallel Simulator (LAMMPS) [49]. The NiCoCrFe HEA simulation cell was constructed by creating a random mixture of elements in a well-defined face-centered cubic (FCC) crystal, which contained Ni, Co, Cr, and Fe elements in an equimolar ratio. Primary knock-on atoms (PKAs) with energies  $E_{\text{PKA}}$  of 10, 20, 30, 40 and 50 keV were modeled within each simulation box, consisting of

$60a_0 \times 60a_0 \times 60a_0$  unit cells (864000 atoms) for the  $E_{\text{PKA}}$  of 10 keV,  $80a_0 \times 80a_0 \times 80a_0$  (2048000 atoms) for 20 keV and 30 keV, and  $100a_0 \times 100a_0 \times 100a_0$  (4000000 atoms) for 40 keV and 50 keV. According to the present interatomic potential, the equilibrium lattice parameter ( $a_0$ ) of 3.52 Å was used for pure Ni, which is close to the experimental values ( $\sim 3.52$  Å for Ni [35]). For the NiCoCrFe HEA, the initial  $a_0$  was determined to be the minimum energy position in the plot showing the internal energies versus the various lattice constants of a crystal under investigation, where the internal energies of the crystal for different lattice constants were calculated with energy minimization, i.e. the conjugate gradient method (see Fig. S1 in the Supplementary Materials). Since  $a_0$  slightly varies with the randomly distributed NiCoCrFe HEAs, it is determined to be 3.58 Å by averaging over 10 NiCoCrFe HEAs with randomly mixed elements in a FCC crystal, which is close to the value obtained in experiment [50]. However, it should be noted that the lattice parameter may be altered due to the local distortion at a raised temperature. To understand how the local distortion affects the lattice parameter, we further carry out the 30 ps MD relaxation (with an isothermal-isobaric (NPT) ensemble at 300 K at which a displacement cascade is simulated: see below). It has been noted that there are some local distortions in the initially FCC lattice for the NiCoCrFe HEA, but the distortions are relatively small and can be neglected. For example, we compared the atomic pair distance between individual atoms before and after energy minimization and MD relaxation, thus demonstrating the relative small effect of the lattice distortion in the NiCoCrFe HEA (see Fig. S2 in the Supplementary Materials). As for a perfect FCC lattice before energy minimization and MD relaxation, the distance of the nearest X-X pairs (X represents Ni, Co, Cr and Fe) is  $\sqrt{2}/2 a_0$  (2.53 Å for the NiCoCrFe HEA based on the  $a_0$  determined above). After energy minimization and MD relaxation, it is observed that the distance of nearest Cr-Cr pairs increases to 2.57 Å, which is the largest, and the distance of the nearest Cr-Co pairs decreases to 2.50 Å, which is the smallest. This lattice distortion in NiCoCrFe HEA is relatively small because Fe, Co, Ni and Cr have a similar atomic radius with a difference  $< 0.8\%$ . Recent researches [51,52] also reported that NiCoCrFe HEA exhibited a negligible lattice distortion as compared with other Ni-based alloys (such as NiCoCr and NiCoCrFeMn HEAs), which is in good agreement with our simulations.

For comparison, the pure Ni simulation cells, with a FCC crystal, were in the same sizes as well. Three-dimensional periodic boundary conditions were imposed to model the bulk materials. A Nose-Hoover thermostat [53] was applied on the outermost layer of the box with a thickness of approximately 3 lattice units to regulate the atomic velocities based on the target temperature.

Prior to initiating a cascade, the supercell energy was minimized using the conjugate gradient method and further equilibrated using MD simulations with an NPT ensemble for 30 ps at 300 K to achieve an equilibrium phonon state. This initial atom supercell was then used as a starting point for the cascade simulation and a reference for the defect analysis. The displacement cascades were initiated by a randomly chosen Ni atom, also called PKA, in each simulation cell with a kinetic energy that ranged from 10 to 50 keV, and the high-index recoil directions of [1] [3] [5] were selected to avoid channeling [54]. The evolution of the displaced atoms during the cascade was followed for approximately 10 ps in pure Ni and 20 ps in the NiCoCrFe HEA. However, the temperature of the cell requires much longer time to cool down, so we extended the simulation time up to 140 ps until no significant changes occurring in each cell.

During the displacement cascade process, simulations were performed under the microcanonical (NVE) ensemble for all the atoms; however, three atomic lattice layers at the boundaries were maintained under the canonical (NVT) ensemble at 300 K.

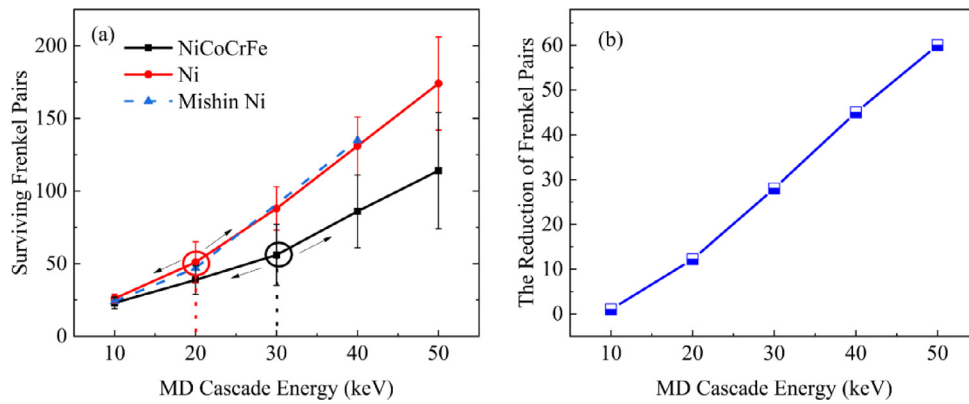


**Fig. 1.** (a) Number of surviving Frenkel pairs at different  $E_{PKA}$  in pure Ni and NiCoCrFe and (b) the reduction of Frenkel pairs in NiCoCrFe at different  $E_{PKA}$ . The reduction of Frenkel pairs is defined as the difference between the number of surviving Frenkel pairs in pure Ni and that in the NiCoCrFe HEA. The numbers shown in the figures are averaged over 20 cascade simulations with a duration of 140 ps.

A variable-time-step algorithm was employed to allow for a small value early in the collision phase and a large value when the energy exchange between atoms declined to thermal levels (general from 0.0001 to 1 fs) [54]. For each simulation cell, including NiCoCrFe and pure Ni, 20 cascades were simulated to generate meaningful statistics, which resulted in a total number of cascades of 200. The 20 cascades in the NiCoCrFe HEA were initiated in 20 random metastable structures and the 20 PKA positions in pure FCC Ni were chosen randomly.

The potentials selected in the current study were the modified embedded-atom method (MEAM) potentials developed by Choi et al. [55]. These potentials can well reproduce the atomic-level phenomena and a number of properties in Ni-based HEAs [38,56,57]. At short distances, the potentials were also corrected by adding the Ziegler-Biersack-Littmark (ZBL) repulsive potential to accurately describe the short-range interactions [58].

## 2.2. Defect analysis

We used the open-source application OVITO [59] for the defect analysis and visualization of simulation results. The Wigner-Seitz method was used to identify vacancies, interstitials and antisites [60]. The lattice sites with empty Wigner-Seitz cells were labeled as vacancies, and the sites occupied by multiple atoms were labeled as interstitials. If an atom occupies a site which previously occupied by another atom type, an antisite defect was defined. However, the antisite defects are formed quickly during the collision (and thermal spike) stages and then they are nearly immobile, i.e. their "evolution" is nearly impossible. It is therefore correct that they do not play any role in defect kinetics, in contrast to vacancies and interstitials. In the current simulations, we mainly focus on the generation and evolution of vacancies and interstitials, and the details of antisite defects can be found in the Fig. S3 in Supplementary Materials. Furthermore, the sizes of the defect clusters involved in this study were determined based on the net defect count, which was the result of the difference between the number of interstitials and vacancies in the cluster. We treated two or more vacancies and interstitials agglomeration as clusters. The clusters with net defect count between 2 and 50 were defined as intermediate-size clusters and the ones with net defect count more than 50 were defined as large-size clusters. The defect size defined in present study is the same as that in the Ullah et al.'s investigation [39]. Finally, the stacking-fault parallelepipeds and stacking-fault tetrahedrons (SFTs) were identified by a combined method of the dislocation extraction algorithm (DXA) [61] and common neighbor analysis (CNA) [62,63]. The dislocation loops and dislocation lines were identified by DXA. The atoms within the stacking-

fault regions and strained regions associated with the dislocation lines [64] were identified by the CNA algorithm.

## 3. Results

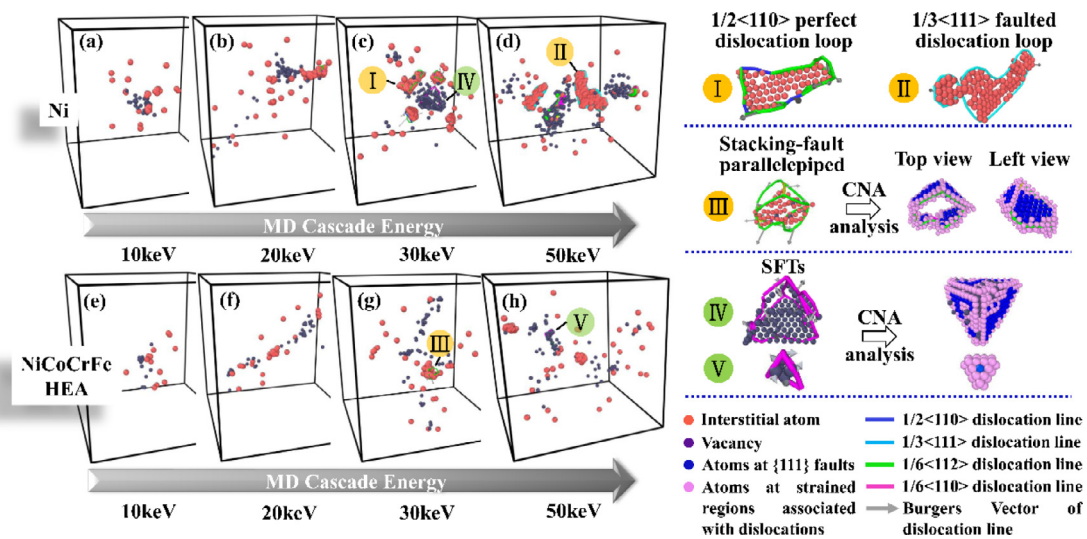
### 3.1. Frenkel pair generation

Fig. 1 (a) presents the final number of Frenkel pairs (FPs) that survived at the end of the cascade simulation (140 ps) in both the NiCoCrFe HEA and pure Ni as a function of  $E_{PKA}$  (from 10 keV to 50 keV). We use term "FPs" to show the number of vacancies, which is obtained from Wigner-Seitz analysis and is equal to the number of interstitials. Prior to investigating the difference between the NiCoCrFe HEA and pure Ni, we primarily verify our simulation results for pure Ni by comparing with the results of Béland et al. [65] that were obtained via the potential of Mishin [66], which is also shown in Fig. 1 (a). Evidently, the results are in good agreement with Béland et al.'s results for the surviving FPs in pure Ni, as well as the inflection point that occurs at 20 keV. According to the analysis of Setyawan et al. [67], this inflection is defined as the threshold energy for the formation of large interstitial clusters (containing 50 or more interstitials in pure Ni [39]). By comparison, the NiCoCrFe HEA presents fewer surviving FPs than pure Ni at each  $E_{PKA}$ . The transition energy for the formation of large interstitial clusters is 30 keV for NiCoCrFe HEA, which is higher than that of pure Ni. This result suggests that both the accumulation of FPs and clustering of interstitials in the NiCoCrFe HEA are inhibited, when compared with that of pure Ni.

The FPs inhibition in the NiCoCrFe HEA is apparent for different  $E_{PKA}$  values, but the inhibited degree varies. To demonstrate this, we define the FPs reduction ( $\delta$ ) to be the difference between the number of surviving FPs in pure Ni and that in the NiCoCrFe HEA. The  $\delta$  in the NiCoCrFe HEA is plotted as a function of  $E_{PKA}$  in Fig. 1 (b). It is clearly seen that  $\delta$  increases linearly with  $E_{PKA}$ , which indicates that the FPs inhibition in the NiCoCrFe HEA is enhanced with increasing  $E_{PKA}$ , compared with that of pure Ni.

### 3.2. Frenkel pair distribution

Fig. 2 presents the distributions of surviving FPs at the end of displacement cascades (140 ps) for the pure Ni (a-d) and the NiCoCrFe HEA (e-h). To produce sufficient defect types for characterization, we chose different  $E_{PKA}$  values from 10 keV to 50 keV. The interstitials and vacancies are represented by large red spheres and small purple spheres, respectively. We primarily focus on interstitial clustering and their size distribution.



**Fig. 2.** Snapshots of defect distributions at the end of displacement cascades (140 ps) for the pure Ni and NiCoCrFe HEA as a function of  $E_{PKA}$ : (a) Ni-10 keV, (b) Ni-20 keV, (c) Ni-30 keV, (d) Ni-50 keV, (e) NiCoCrFe-10 keV, (f) NiCoCrFe-20 keV, (g) NiCoCrFe-30 keV, (h) NiCoCrFe-50 keV. Detailed views of dislocation loops (I-II), stacking-fault parallelepiped (III) and SFTs (IV-V) are provided.

In both cases, the number of interstitials in clusters generally increases with increasing  $E_{PKA}$ . At 10 keV, most of the interstitials are single interstitials, as shown in Fig. 2 (a) and (e) for Ni and the NiCoCrFe HEA, respectively. When  $E_{PKA}$  increases to 20 keV (Fig. 2 (b) and (f)), there are small interstitial clusters produced, which suggests that single interstitials start to accumulate and form clusters. The formation of interstitial clusters is accelerated as  $E_{PKA}$  further increases (Fig. 2 (c), (d), (g) and (h)). It is observed that large interstitial clusters start to form dislocation loops. The detailed analysis of these interstitial dislocation loops reveals that most of them are  $1/2\langle 110 \rangle$  dislocation loops (so-called perfect dislocation loops) and  $1/3\langle 111 \rangle$  dislocation loops (so-called faulted dislocation loops), as shown in Fig. 2 (c) and (d). Previous studies have also observed the  $1/2\langle 110 \rangle$  perfect loops and  $1/3\langle 111 \rangle$  faulted loops in irradiated Ni and Ni-based alloys either by transmission electron microscopy (TEM) [15,31,68,69] or by MD simulations [25,27,39,70]. In addition, we observed the stacking-fault parallelepipeds (with faces lying on several sets of {111} planes), but only in the NiCoCrFe HEA, which are formed by several  $1/6\langle 112 \rangle$  dislocations (so-called partial dislocations) (see Fig. 2 (g)). The atoms lying on stacking-fault regions ({111} planes) are represented by blue spheres, and the atoms located in the strained regions associated with dislocation lines are represented by pink spheres. Similar structures have also been observed in the NiCoCrFeMn HEA according to earlier research [68], which indicates that more types of dislocation structures can be formed in HEAs than in pure metal.

The direct examination of Fig. 2 shows that both the size and number of interstitial clusters in NiCoCrFe are smaller than those in pure Ni for all the  $E_{PKA}$  considered. This result indicates that the kinetics of interstitial clustering is restrained in NiCoCrFe, when compared to that in pure Ni. However, it is found that the inhibited effects on cluster formation are different and depend on  $E_{PKA}$ . The distributions of the number of interstitials in clusters with different size for the four  $E_{PKA}$  are shown in Fig. 3 (a) – (d). In present study, we defined the defect size in detail at Section 2.2. The inhibited effects on interstitial clustering in the NiCoCrFe HEA can be clearly observed. For example, the number of single interstitials in pure Ni is almost the same as that in the NiCoCrFe for all the  $E_{PKA}$  simulated. However, the total number of interstitials (or FPs) in pure Ni is significant higher than that in the NiCoCrFe (see Fig. 1), suggesting that more interstitials are incorporated in the

interstitial clusters in pure Ni and demonstrating that the interstitial clustering is restrained in the NiCoCrFe. Second, the number of interstitials in large-size clusters ( $>50$ ) increases with  $E_{PKA}$  in both materials, but faster in pure Ni. For example, in the case of 10 keV (Fig. 3 (a)), there are no large-size clusters in both materials. When  $E_{PKA}$  increases to 20 keV (Fig. 3 (b)), 14 % interstitials begin to form large clusters in pure Ni, while there are still no interstitials accumulating into large clusters in the NiCoCrFe HEA (as shown in Fig. 3(b)). As  $E_{PKA}$  further increases from 30 keV to 50 keV, there are nearly 40% interstitials forming large clusters in pure Ni (Fig. 3 (d)); but in contrast, most of interstitials in the NiCoCrFe still remain in the intermediate size (between 2 and 50) clusters and only 15% interstitials are segregated into large clusters. The lower fraction of interstitials in large clusters and fewer survival defects in the NiCoCrFe HEA result in the smaller average size of interstitial clusters in the NiCoCrFe HEA. A detailed comparison of size distribution of interstitial clusters between Ni and the NiCoCrFe HEA is shown in Fig. S4 in the Supplementary Materials. It is observed that the cluster size increases with  $E_{PKA}$  in both materials, and pure Ni presents more and larger clusters than that of the NiCoCrFe. In addition, we observe that the maximum cluster size ( $R_{max}$ ) in the NiCoCrFe HEA tends to saturate when  $E_{PKA}$  increases from 30 keV to 50 keV, but the  $R_{max}$  in pure Ni continuously increases without saturation (See Fig. S5 in the Supplementary Materials).

The delayed formation of large defect clusters in the NiCoCrFe HEA clearly indicates that 30 keV is the transition energy for the inhibited clustering to occur, compared with that in pure Ni. In addition, the  $E_{PKA}$  at which the dislocation loops begin to form is different for both materials. It is found that the formation of large dislocation loops begins at 20 keV in pure Ni, but it starts at 30 keV in the NiCoCrFe HEA, which is also consistent with the transition energy that is demonstrated in Fig. 1 (a). The growth inhibition of interstitial clusters (loops) in the NiCoCrFe HEA in the present work is also supported by the recent researches, including both experiments [15,22,26] and simulations [11,25,27,38,39]. Using MD simulations, Ullah et al. [39] reported that the interstitial cluster in pure Ni was able to increase to a huge size ( $> 400$ ) with increasing dose, while it always remained small in the HEA. In experiment, Lu et al. [15,22] also observed that the size of loops increased with increasing irradiation dose in pure Ni, but the loop growth was



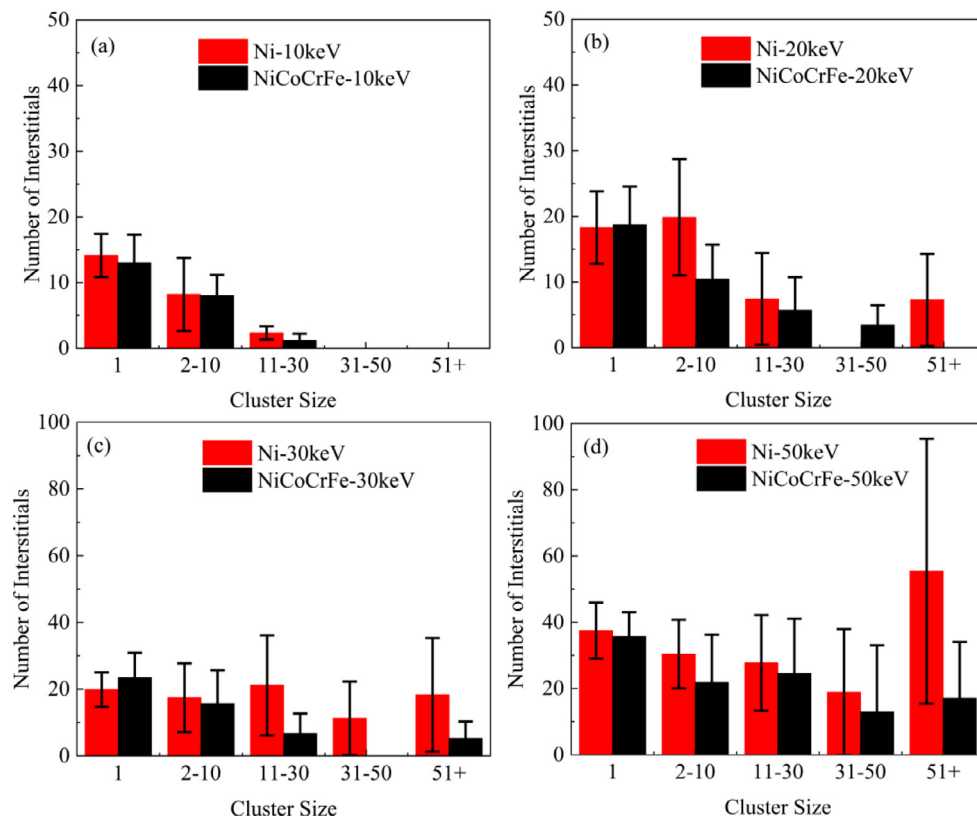


**Fig. 3.** Number of interstitials in clusters of different sizes for pure Ni and the NiCoCrFe HEA after (a) 10 keV, (b) 20 keV, (c) 30 keV and (d) 50 keV displacement cascade simulations. The numbers shown in the figures are averaged over 20 cascade simulations with a duration of 140 ps.

delayed in the NiCoCrFe HEA. These results agree well with our observations.

However, a higher density of interstitial loops has been observed in the irradiated NiCoCrFe HEA by experiments [15,22], which is not observed in the present simulations. Instead, there are less number of interstitial clusters (loops) in the NiCoCrFe HEA (see Fig. S4). There might be several reasons accounting for the lower loop densities. Firstly, the large difference in the irradiation doses between the present simulations ( $\sim 0.0075$  dpa of maximum dose estimated based on defect production in single cascades) and experiments (38 dpa in Ref. [15]) could cause the different densities of interstitial clusters. With the increase in dose, it is likely that the accumulation of defect clusters will be dominated by the increase in their number densities rather than size growth. Secondly, there are different timescales between simulations and experiments. It is well known that the motion and interaction of dislocation loops during defect evolution can lead to a different distribution of dislocation loops. Similar to the results of previous studies [26,27,68,69], our simulations revealed that the dislocation loops in HEAs have a limited mobility, when compared with those in pure Ni, and can be trapped by different atoms in the loops. For example, only a few jumps of the dislocation loops in the NiCoCrFe HEA are observed for an extended MD simulation (up to 8 ns) at 800 K. The suppressed mobility of dislocation loop can maintain a high dislocation density and increases the incubation period that continues during the further evolution of dislocation loops [71]. Overall, the differences in both irradiation dose and timescales should be two of the main reasons for the different densities of interstitial loops observed in the NiCoCrFe HEA between the present simulations and experiments.

Similar to the interstitials case, the number of vacancies in clusters generally increases with increasing  $E_{PKA}$  in both cases, and the

large vacancy clusters are only formed at higher  $E_{PKA}$  (see Fig. 2). It is observed that some vacancy clusters start to form SFTs, as shown in Fig. 2 (c) and (h). The detailed analysis of these SFTs reveals that they comprise of six  $1/6\langle 110 \rangle$  dislocations (so called stair-rod dislocations), presenting the shape of a tetrahedron with four  $\{111\}$  faces. These SFTs have previously been observed in irradiated Ni and Ni-based alloys either by TEM [31,50,72] or by MD simulations [11,25].

Although the total number of vacancies is less in the NiCoCrFe HEA than that in pure Ni, which is similar to the case with interstitials, the distributions of vacancies are different. The distributions of the number of vacancies in clusters with different sizes for the four  $E_{PKA}$  are shown in Fig. 4. It can be clearly seen that the number of vacancies in clusters increases with increasing  $E_{PKA}$  in both materials. In comparison, there are fewer single vacancies and more vacancies in intermediate-size clusters (between 2 and 50) in the NiCoCrFe HEA than that in pure Ni for all the  $E_{PKA}$  considered. However, there are no vacancies forming large-size clusters ( $>50$ ) in the NiCoCrFe HEA, in contrast to those in pure Ni. For example, in the case of 10 and 20 keV (Fig. 4 (a), and (b)), the vacancies mostly remain as single vacancies and intermediate vacancy clusters in both materials. As  $E_{PKA}$  increases from 30 keV to 50 keV, the vacancies that form large clusters can only be observed in pure Ni (Figs. 4 (c) and (d)). These results indicate that the vacancies in the NiCoCrFe HEA tend to form intermediate-size clusters rather than large-size clusters. A detailed comparison of size distribution of vacancy clusters between both materials is provided in Fig. S6 in the Supplementary Materials. In Fig. S6, it is clearly observed that the size and number of vacancy clusters increases with  $E_{PKA}$  in both materials. In comparison, there are more intermediate-size clusters but fewer large-size clusters in the NiCoCrFe HEA than in pure Ni for all the  $E_{PKA}$  considered. Overall, compared with pure

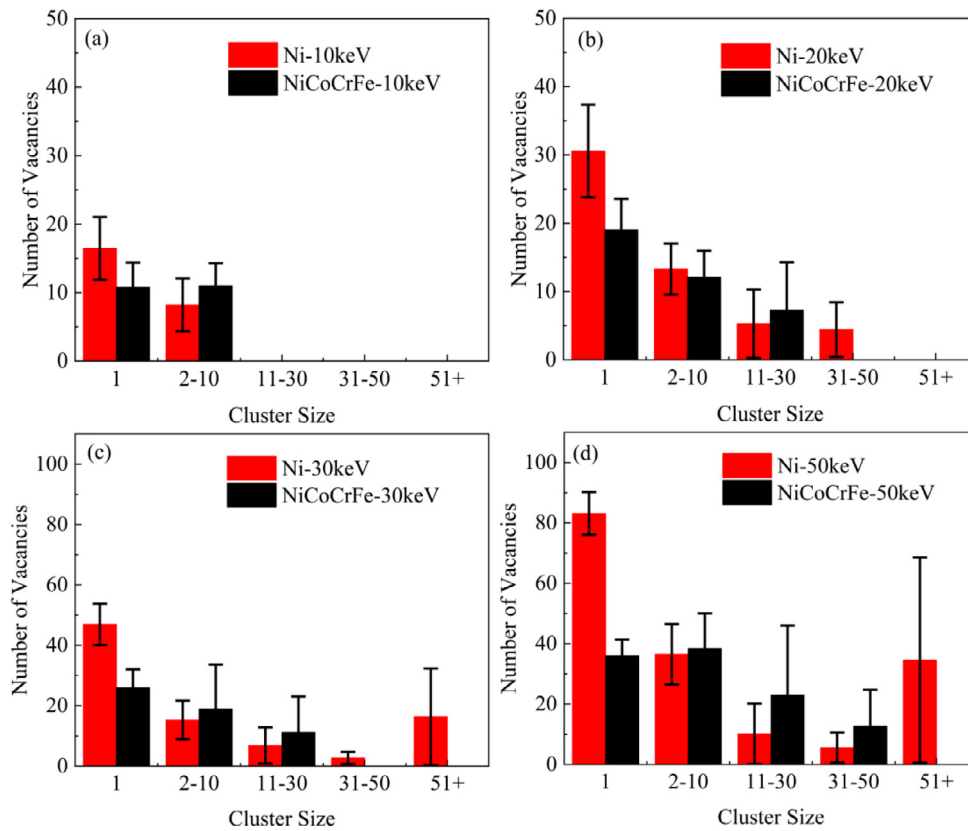


**Fig. 4.** Number of vacancies in clusters of different sizes for pure Ni and NiCoCrFe HEA after (a) 10 keV, (b) 20 keV, (c) 30 keV and (d) 50 keV displacement cascade simulations. The numbers shown in the figures are averaged over 20 cascade simulations with a duration of 140 ps.

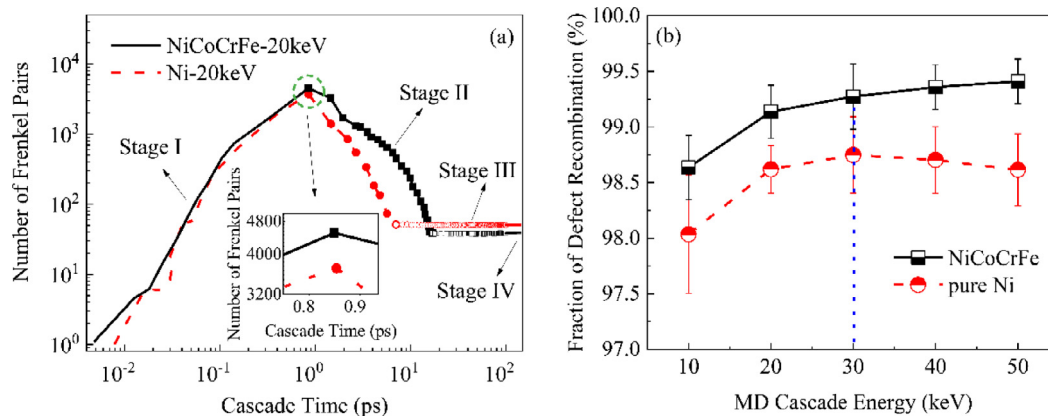


**Fig. 5.** (a) The number of Frenkel pairs as a function of simulation time for the NiCoCrFe and pure Ni during cascade simulation in the case of  $E_{PKA}=20$  keV. (b) The fractions of defect recombination in two materials as a function of  $E_{PKA}$ . The inset in (a) shows the difference in the damage peaks between Ni and the NiCoCrFe. The numbers shown in the figures are averaged over 20 cascade simulation with a duration of 140 ps.

Ni, the NiCoCrFe HEA exhibits a higher density of intermediate vacancy clusters (including SFTs), which is in good agreement with experimental observations [15,32]. These results indicate that the formation of large vacancy clusters is inhibited in the NiCoCrFe HEA.

### 3.3. Frenkel pair evolution

To examine how FPs evolve in both materials, the variations in displaced atoms are analyzed during different stages. Taking the 20 keV case as an example, the process of the cascade formation in NiCoCrFe and pure Ni by monitoring the number of FPs as a

function of simulation time is shown in Fig. 5 (a). Similar to the previous study, the cascade formation process can be categorized into four stages. There is a rapid buildup in the number of FPs during the initial collision phase that is defined as stage I in Fig. 5 (a), and then, the number of FPs reaches a maximum value, forming a so-called thermal spike. Subsequently, most of the FPs recombine and are annihilated during the relaxation of thermal spike (defined as stage II), leaving only a few surviving FPs behind. Then, the surviving FPs further evolve in remaining stage of primary damage (referring to stage III) and the stage of thermal defect migration (namely, stage IV) [48]. By comparison, NiCoCrFe presents more FPs at the peak (thermal spike), but fewer surviving FPs after re-

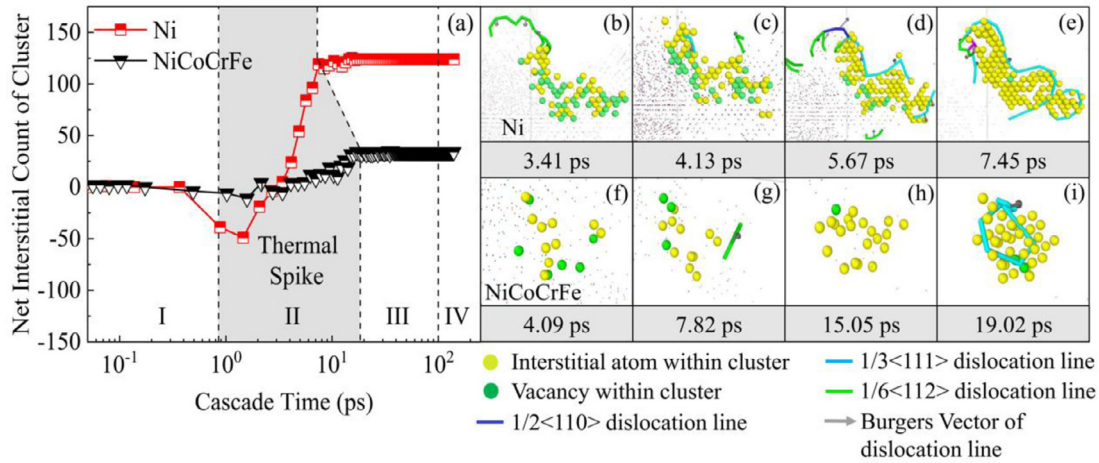


**Fig. 6.** (a) The evolution of net interstitial count within an interstitial cluster for both materials during cascade simulation in the case of  $E_{PKA}=50$  keV. The net interstitial count equals the number of interstitials minus the number of vacancies in the cluster. A series of snapshots of defects within the interstitial cluster in pure Ni (b)–(e) and the NiCoCrFe HEA (f)–(i) during the cascade evolution are provided.

combination, than pure Ni. For example, the number of FPs at the peak in NiCoCrFe is 4498 for a 20 keV cascade, while only 3695 FPs are formed in pure Ni. However, the number of surviving FPs in the NiCoCrFe HEA is 39, which is lower than that of pure Ni (51). As a result, the recombined FPs in NiCoCrFe (4459) is higher than that in pure Ni (3644). The more FPs at the peak and the fewer surviving FPs at the end of the cascades suggest that one of the key roles controlling FPs reduction in the NiCoCrFe HEA is a high recombination rate during stage II.

The recombination fractions of FPs ( $\xi$ ) in NiCoCrFe and pure Ni for all  $E_{PKA}$  considered are shown in Fig. 5 (b), where  $\xi$  is the ratio of recombined FPs ( $N_r$ ) to FPs at the peak ( $N_p$ ). By comparison, the  $\xi$  in the NiCoCrFe HEA is higher than that in pure Ni for all  $E_{PKA}$  simulated. In pure Ni, it is observed that the  $\xi$  increases with increasing  $E_{PKA}$  at lower energies (10 to 30 keV), but slightly decreases after 30 keV. However, the  $\xi$  for the NiCoCrFe HEA monotonously increases with increasing  $E_{PKA}$ . This indicates that the difference between the NiCoCrFe HEA and pure Ni diverges at 30 keV and then increases with increasing  $E_{PKA}$ , which is similar to the transition energy trend for the clustering inhibition in the NiCoCrFe HEA. For example, the largest difference between the NiCoCrFe HEA ( $\xi=99.4\%$ ) and pure Ni ( $\xi=98.6\%$ ) is approximately 1% (at 50 keV), which indicates the difference in the number of recombined defects between the NiCoCrFe HEA ( $N_r=19209$ ) and pure Ni ( $N_r=12388$ ) is 6821, approximately 7 times larger than that at 30 keV (990). The different increase rates of  $\xi$  between both materials indicate that the mechanisms affecting the defect recombination are different in different energy regimes.

A distinct feature near the transition energies is the formation of large-size interstitial clusters in both materials. Therefore, it is necessary to understand in detail the interstitial cluster formation within the cascade evolution. The number of net interstitials in a defect cluster of both materials as a function of simulation time at  $E_{PKA}=50$  keV is shown in Fig. 6, where the net interstitial count ( $N_{int}$ ) is defined as the number of interstitials minus the number of vacancies in the cluster. For both materials,  $N_{int}$  decreases at first during stage I and reaches to a minimum value in the beginning of stage II, which is indicated by the shaded area in Fig. 6 (a). In the duration of stages III and IV,  $N_{int}$  reaches a stable value. For comparison, NiCoCrFe shows a slower increase in  $N_{int}$  than does pure Ni during stage II and presents a smaller value at stages III and IV. In addition, it is of interest to note that the formation of dislocations and dislocation loops in pure Ni occurs at the begin-

ning of stage II (as shown in Fig. 6 (b)–(e)). The atom information of the interstitial cluster is highlighted with yellow for interstitials and green for vacancies. These dislocations are identified as  $1/6\langle 112 \rangle$  partial dislocations (in green),  $1/2\langle 110 \rangle$  perfect dislocations (in blue),  $1/3\langle 111 \rangle$  faulted dislocations and loops (in cyan). It is observed that a  $1/2\langle 110 \rangle$  perfect dislocation can dissociate into two  $1/6\langle 112 \rangle$  partial dislocations at its end (see Fig. 6 (d)), which is in agreement with earlier studies [68,69]. However, the loop formation in the NiCoCrFe HEA does not occur until the end of stage II (Fig. 6 (f)–(i)). These results suggest that the formation of dislocation loops in pure Ni occurs considerably earlier than it does in the NiCoCrFe HEA, which inhibits the recombination of FPs and reduces the recombination rate. Similar mechanisms for how dislocation loops absorb adjacent defects and, in turn, inhibit defect recombination have been suggested in earlier research [64], which strongly supports our findings. The delayed nucleation of interstitial clusters in the NiCoCrFe HEA, compared with that in pure Ni, may provide enough time for interstitials to migrate and recombine with vacancies, which inhibits the decrease in  $\xi$  (see Fig. 5 (b)).

In contrast to interstitials, the mobility of vacancies is much lower; therefore, it is very difficult to observe the migration of vacancies at MD timescales. Aidhy et al. [25] have reported that the vacancies are completely immobile until 700 K and start to diffuse at approximately 1000 K in pure Ni on MD timescales. In our simulations, we only observed a few migrations of certain vacancies within the cascade core. However, it is observed that the transformation of vacancy clusters into SFTs occurs frequently at the cores of cascades, which also inhibits the migration of vacancies.

## 4. Discussion

As described above, the higher FPs recombination in NiCoCrFe significantly affects the defect evolution, compared with that in pure Ni. The change in recombination efficiency with  $E_{PKA}$  presents a competition between defect production and FPs annihilation, which is associated with the multiple mechanisms involved in a cascade. Thus, two possible mechanisms are proposed here to interpret the higher FPs recombination in NiCoCrFe.

### 4.1. The lifetime of thermal spike

It is well known that FPs recombination is strongly correlated with the diffusion coefficients of interstitials and vacancies, which

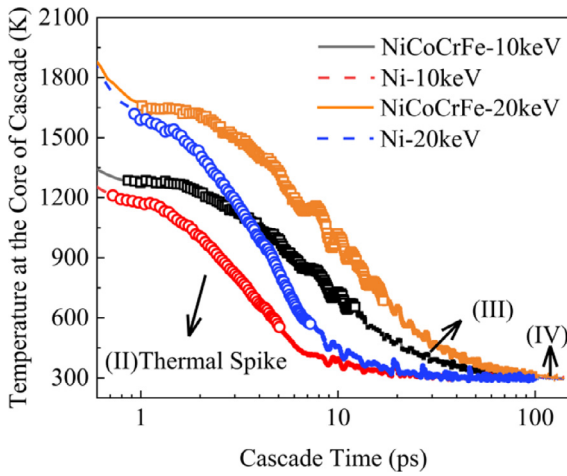


Fig. 7. The evolution of temperatures at the core of cascade in NiCoCrFe and pure Ni with time during cascade simulations in the cases of  $E_{PKA}$ =10 keV and 20 keV.

is influenced by the temperature [73]. Thus, we compare the temperatures of the cascade core within the simulation cells for two materials at the energies of 10 and 20 keV, as shown in Fig. 7. The temperature in the thermal spike was calculated by the formula  $K = 3Nk_B T/2$  within the cascade volume, where  $K_E$  = total kinetic energy of the atoms within the volume ( $\sum_{i=1}^N m_i v_i^2/2$ ),  $N$  = number of atoms within the volume,  $k_B$  = Boltzmann constant, and  $T$  = temperature. Both  $K_E$  and  $N$  were obtained by the LAMMPS codes. At both PKA energies, the temperature decreases and reaches room temperature (300 K) in both materials from stage II to IV. At stage II, which corresponds to the so-called thermal spike of a cascade, the temperature quickly decreases in pure Ni (red and blue lines). Similarly, the temperature at stage II decreases in NiCoCrFe (black and yellow lines), but its lifetime (thermal spike) is much longer than that in pure Ni. It should be noted that the lifetime of thermal spike is defined by the time when majority of displaced atoms (or FPs) recombine and survival defects are essentially stable [48,74]. For example, the lifetime of the thermal spike at 20 keV in the NiCoCrFe is estimated to be 16.98 ps, but it is only approximately 7.04 ps in Ni (see Fig. 5 (a)). The considerably longer high temperature period within the cascade and the thermal spike lifetime in NiCoCrFe compared to those in pure Ni could significantly enhance the recombination of FPs. In the case of 10 keV, the temperatures at stage II are all lower than those at 20 keV for both materials, and the delayed decreases in temperature at stage II for NiCoCrFe are less significant than that at 20 keV. Nevertheless, the final temperature in the NiCoCrFe HEA at the end of 140 ps does not reach 300 K in the case of 30 keV to 50 keV and may require longer time to cool down. The results indicate that NiCoCrFe exhibits a substantially longer lifetime of the thermal spike than pure Ni at a higher  $E_{PKA}$ .

In general, the temperature decreases soon after the cascade because there is a 300 K temperature-controlled layer at the boundary of simulation cells. The longer lifetime at stage II in the NiCoCrFe HEA may be associated with its lower thermal conductivity than that of pure Ni. It has been reported that the thermal conductivity of the NiCoCrFe HEA is less than  $8 \text{ W}\cdot\text{m}^{-1}\text{K}^{-1}$ , while it is more than  $100 \text{ W}\cdot\text{m}^{-1}\text{K}^{-1}$  [35] for pure Ni, approximately 13 times larger. As a result, the heat dissipation in the NiCoCrFe HEA is retarded, leading to a long-lasting thermal spike phase, which also increases with increasing  $E_{PKA}$ . The longer high temperature process at the core of the cascade is able to accelerate the migration of interstitials and vacancies, which could be one of the reasons for the higher  $\xi$  in the NiCoCrFe HEA. Similar to the case of

Table 1

The comparison of formation energies and binding energies (eV) in pure Ni between our simulation results and others'.

	$E_f$ (I)	$E_f$ (V)	$E_b$ (I-V) (1nn)
Present	4.92	1.51	0.18
MD simulation			0.201 [76]
Ab initio calculation	4.27 [77]	1.47 [77]	0.04 [76]
Theo.	4.07 [78]	1.43 [78], 1.46 [79]	
Expt.		1.58–1.63 [80], 1.8 [81]	

10 and 20 keV, the longer lifetimes of the thermal spike at higher energies can be also applied to explain the enhanced FPs recombination in the NiCoCrFe HEA for all  $E_{PKA}$  considered. However, it should be noted that the decrease in the  $\xi$  of pure Ni for  $E_{PKA}$  above 30 keV (as shown in Fig. 5 (b)), which is different with that of NiCoCrFe HEA, indicating there are other mechanisms affecting the FPs recombination in both materials at higher energies.

#### 4.2. Binding energy of interstitial clusters

To understand the delayed interstitial clustering of the NiCoCrFe HEA, we compared the differences in the binding energies of interstitial clusters between the two materials. The total binding energy of an interstitial cluster with  $n$  interstitials can be directly calculated from its formation energy and is defined as the energy difference between the system where all the interstitials interact and the system where all the interstitials are well separated from each other without any interaction. Thus, the total binding energy for a loop containing  $n$  interstitials is defined as:

$$E_b^{d_1, d_2, \dots, d_n} = \sum_{i=1}^n E_f^{d_i} - E_f^{d_1, d_2, \dots, d_n} \quad (1)$$

where  $E_f^{d_i}$  is the formation energy of the system containing defect  $d_i$  only and  $E_f^{d_1, d_2, \dots, d_n}$  is the formation energy of a defect cluster with  $n$  interacting interstitials [75].

To verify the reliability of our simulations, we first calculate the formation energies and binding energies of the interstitials and vacancies in Ni and compare the values with the results in the literature. Generally, the values in our simulations are in good agreement with previous calculations [76–81] (see Table 1). In the present study, both  $1/3\langle 111 \rangle$  faulted dislocation loops and  $1/2\langle 110 \rangle$  perfect dislocation loops are considered, which have drawn considerable attention recently. The binding energies of interstitial clusters and dislocation loops as a function of size are shown in Fig. 8. For both interstitial clusters and dislocation loops, the total binding energy increases with the increasing size of both materials. However, it is of interest to note that the binding energy of loops in pure Ni is larger than that in the NiCoCrFe HEA, and the difference between them increases with the loop size. For each material, the binding energy of  $1/2\langle 110 \rangle$  perfect loops (Fig. 8 (a)) is less than that of  $1/3\langle 111 \rangle$  faulted loops (Fig. 8 (b)). These results suggest that the dislocation loops can form more easily in pure Ni than in the NiCoCrFe HEA, which should be one of the main reasons for the inhibited interstitial clustering observed in the NiCoCrFe HEA. The similar comparison of binding energies between defects is also used to judge the relative stability of defect formations [75]. The higher binding energy of  $1/3\langle 111 \rangle$  faulted loops explains why their population is higher than that of  $1/2\langle 110 \rangle$  perfect loops in the current simulations. Furthermore, experiments have demonstrated that the friction of  $1/3\langle 111 \rangle$  faulted dislocation loops is higher than that of  $1/2\langle 110 \rangle$  perfect loops in pure Ni at low irradiation doses [15], which agrees with our results. The smaller driving force for clustering or loop formation in NiCoCrFe is due to the smaller binding energy of in-



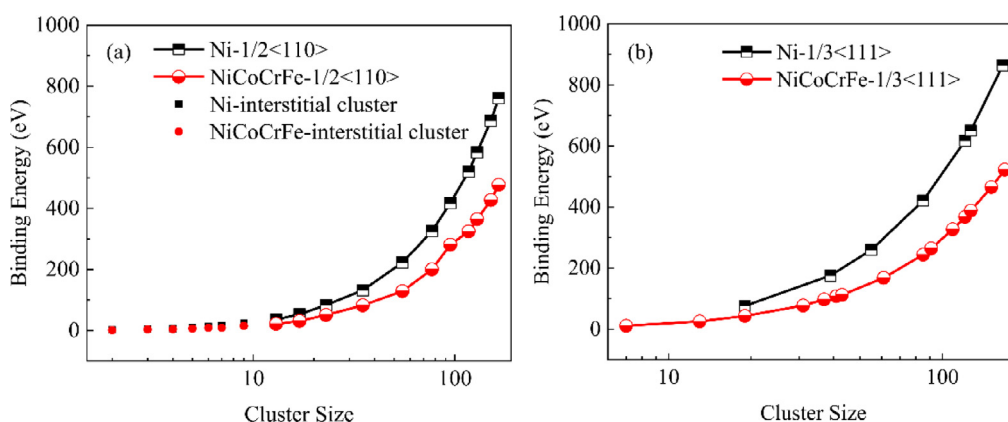


**Fig. 8.** The binding energy of interstitial cluster and dislocation loop for both materials: (a) small interstitial cluster and  $1/2\langle 110 \rangle$  perfect interstitial loop; (b)  $1/3\langle 111 \rangle$  faulted interstitial loop.

terstitials, compared to that in pure Ni, thus increasing the probability for FPs to recombine in NiCoCrFe when compared with pure Ni above 30 keV.

The resistance to defect production in the NiCoCrFe HEA has been investigated using MD simulations with the recently developed MEAM potentials. When compared with the pure Ni, the enhanced thermal spike, long-lasting high temperature at the core of cascades, low thermal conductivity and small binding energy of interstitials in the NiCoCrFe HEA may account for the observed phenomenon. When  $E_{PKA}$  is low, the  $\xi$  in both materials increases at the same rate because there are no large dislocation loops forming in either material. Therefore,  $\xi$  is mainly influenced by the enhanced thermal spike in both materials. As  $E_{PKA}$  increases up to 30 keV, the increase rate of  $\xi$  differs for different materials because there are overwhelming dislocation loops that form in pure Ni, compared with the NiCoCrFe HEA; this action significantly inhibits the FPs recombination, thus leading to the decrease in  $\xi$ . Although the different mechanisms may account for the interstitial clustering within the different  $E_{PKA}$  regions, NiCoCrFe exhibits a high defect reduction, including surviving FPs and defect clusters for all the  $E_{PKA}$  energies considered, thus demonstrating the radiation resistance of HEAs, which has also been observed in experiments.

The sizes of dislocation loops and voids are much smaller in the NiCoCrFe HEA than in the pure Ni, as has been revealed in TEM observations of irradiated HEAs [22] and the current simulations. In addition, we observed the confined migration of a perfect dislocation loop, the formation of stacking-fault parallelepipeds and SFTs in the NiCoCrFe HEA, which is in good agreement with recent experimental results [68,69,72]. These results reveal that our MD simulations are reliable and provide atomic-level knowledge for understanding the irradiation resistance of the NiCoCrFe HEA. However, it should be noted that a direct comparison between experimental and simulation results is difficult due to the different timescale in simulations, which is many orders of magnitude shorter than the experimental timescale. The migration of defects and the interaction between defects may be significant at the late stage of radiation damage. However, the current simulations provide the most basic and primary knowledge for understanding the micromechanisms of defect survival in the NiCoCrFe HEA.

## 5. Conclusion

In the present study, the generation, distribution and evolution of irradiation-induced defects in the NiCoCrFe HEA were investigated by molecular dynamics (MD) simulations to understand the possible mechanisms for the enhanced radiation tolerance in HEAs,

compared with that in pure bulk Ni. The displacement cascades were simulated for the PKA energies ranging from 10 to 50 keV, and the surviving defects are analyzed. The present simulations clearly illustrate that there is a higher defect recombination rate in the NiCoCrFe HEA, compared with that in pure Ni, which is induced by the enhanced thermal spike, lower thermal conductivity and smaller binding energy of interstitials, thus affecting the cascade evolution and resulting in the suppressed damage accumulation in the NiCoCrFe HEA. Additionally, these detailed mechanisms are the key factors that increase the defect recombination efficiency in NiCoCrFe, thus providing significant insights into engineering the microstructures of Ni-based HEAs for radiation tolerance applications.

## Declaration of Competing Interest

None

## Acknowledgments

This work was supported by the National MCF Energy R&D Program (2018YFE0308101) and the National Natural Science Foundation of China (Grant Nos. 11775074, 11905057 and 11935004).

## Supplementary materials

Supplementary material associated with this article can be found, in the online version, at doi:10.1016/j.actamat.2020.06.027.

## References

- [1] W. Li, P.K. Liaw, Y. Gao, Fracture resistance of high entropy alloys: A review, *Intermet* 99 (2018) 69–83.
- [2] Z. Li, K.G. Pradeep, Y. Deng, D. Raabe, C.C. Tasan, Metastable high-entropy dual-phase alloys overcome the strength–ductility trade-off, *Nature* 534 (2016) 227.
- [3] B. Gludovatz, A. Hohenwarter, D. Catoor, E.H. Chang, E.P. George, R.O. Ritchie, A fracture-resistant high-entropy alloy for cryogenic applications, *Science* 345 (2014) 1153–1158.
- [4] Z. Lei, X. Liu, Y. Wu, H. Wang, S. Jiang, S. Wang, X. Hui, Y. Wu, B. Gault, P. Kontis, D. Raabe, L. Gu, Q. Zhang, H. Chen, H. Wang, J. Liu, K. An, Q. Zeng, T.-G. Nieh, Z. Lu, Enhanced strength and ductility in a high-entropy alloy via ordered oxygen complexes, *Nature* 565 (2019) 546–552.
- [5] Z. Wu, H. Bei, G.M. Pharr, E.P. George, Temperature dependence of the mechanical properties of equiatomic solid solution alloys with face-centered cubic crystal structures, *Acta Mater* 81 (2014) 428–441.
- [6] T. Yang, Y.L. Zhao, Y. Tong, Z.B. Jiao, J. Wei, J.X. Cai, X.D. Han, D. Chen, A. Hu, J.J. Kai, K. Lu, Y. Liu, C.T. Liu, Multicomponent intermetallic nanoparticles and superb mechanical behaviors of complex alloys, *Science* 362 (2018) 933–937.
- [7] M.-H. Chuang, M.-H. Tsai, W.-R. Wang, S.-J. Lin, J.-W. Yeh, Microstructure and wear behavior of AlxCo1.5CrFeNi1.5Ti high-entropy alloys, *Acta Mater.* 59 (2011) 6308–6317.

- [8] A. Zhang, J. Han, B. Su, P. Li, J. Meng, Microstructure, mechanical properties and tribological performance of CoCrFeNi high entropy alloy matrix self-lubricating composite, *Mater. Des.* 114 (2017) 253–263.
- [9] V.G. Gavriljuk, B.D. Shanina, H. Berns, Ab initio development of a high-strength corrosion-resistant austenitic steel, *Acta Mater* 56 (2008) 5071–5082.
- [10] A. Ayyagari, V. Hasannaeimi, H. Grewal, H. Arora, S. Mukherjee, Corrosion, erosion and wear behavior of complex concentrated alloys: a review, *Met* 8 (2018) 603.
- [11] L. Koch, F. Granberg, T. Brink, D. Utt, K. Albe, F. Djurabekova, K. Nordlund, Local segregation versus irradiation effects in high-entropy alloys: Steady-state conditions in a driven system, *J. Appl. Phys.* 122 (2017) 105106.
- [12] O.N. Senkov, G. Wilks, J. Scott, D.B. Miracle, Mechanical properties of Nb<sub>25</sub>Mo<sub>25</sub>Ta<sub>25</sub>W<sub>25</sub> and V<sub>20</sub>Nb<sub>20</sub>Mo<sub>20</sub>Ta<sub>20</sub>W<sub>20</sub> refractory high entropy alloys, *Intermet* 19 (2011) 698–706.
- [13] F. Otto, A. Dlouhý, C. Somsen, H. Bei, G. Eggeler, E.P. George, The influences of temperature and microstructure on the tensile properties of a CoCrFeMnNi high-entropy alloy, *Acta Mater* 61 (2013) 5743–5755.
- [14] M.-H. Tsai, J.-W. Yeh, High-Entropy Alloys: A Critical Review, *Mater. Res. Lett.* 2 (2014) 107–123.
- [15] C. Lu, T. Yang, K. Jin, N. Gao, P. Xiu, Y. Zhang, F. Gao, H. Bei, W.J. Weber, K. Sun, Y. Dong, L. Wang, Radiation-induced segregation on defect clusters in single-phase concentrated solid-solution alloys, *Acta Mater* 127 (2017) 98–107.
- [16] G.S. Was, Z. Jiao, E. Getto, K. Sun, A.M. Monterrosa, S.A. Maloy, O. Anderoglu, B.H. Sencer, M. Hockett, Emulation of reactor irradiation damage using ion beams (vol 88, pg 33, 2014), *Scr. Mater.* 93 (2014) 33–36.
- [17] B.P. Uberuaga, R.G. Hoagland, A.F. Voter, S.M. Valone, Direct transformation of vacancy voids to stacking fault tetrahedra, *Phys. Rev. Lett* 99 (2007) 135501.
- [18] A. Hirata, T. Fujita, Y. Wen, J. Schneibel, C.T. Liu, M. Chen, Atomic structure of nanoclusters in oxide-dispersion-strengthened steels, *Nat. Mater* 10 (2011) 922.
- [19] G.R. Odette, Recent progress in developing and qualifying nanostructured ferritic alloys for advanced fission and fusion applications, *JOM* 66 (2014) 2427–2441.
- [20] W. Han, M.J. Demkowicz, N.A. Mara, E. Fu, S. Sinha, A.D. Rollett, Y. Wang, J.S. Carpenter, I.J. Beyerlein, A. Misra, Design of radiation tolerant materials via interface engineering, *Adv. Mater* 25 (2013) 6975–6979.
- [21] C. Sun, S. Zheng, C. Wei, Y. Wu, L. Shao, Y. Yang, K. Hartwig, S. Maloy, S. Zinkle, T. Allen, Superior radiation-resistant nanoengineered austenitic 304L stainless steel for applications in extreme radiation environments, *Sci. Rep.* 5 (2015) 7801.
- [22] C. Lu, L. Niu, N. Chen, K. Jin, T. Yang, P. Xiu, Y. Zhang, F. Gao, H. Bei, S. Shi, Enhancing radiation tolerance by controlling defect mobility and migration pathways in multicomponent single-phase alloys, *Nat. Commun.* 7 (2016) 13564.
- [23] R. Sachan, M.W. Ullah, M.F. Chisholm, J. Liu, P.F. Zhai, D. Schauries, P. Kluth, C. Trautman, H.B. Bei, W.J. Weber, Y.W. Zhang, Radiation-induced extreme elastic and inelastic interactions in concentrated solid solutions, *Mater. Des.* 150 (2018) 1–8.
- [24] S.C. Middleburgh, D.M. King, G.R. Lumpkin, M. Cortie, L. Edwards, Segregation and migration of species in the CrCoFeNi high entropy alloy, *J. Alloy. Compd.* 599 (2014) 179–182.
- [25] D.S. Aidhy, C. Lu, K. Jin, H. Bei, Y. Zhang, L. Wang, W.J. Weber, Point defect evolution in Ni, NiFe and NiCr alloys from atomistic simulations and irradiation experiments, *Acta Mater.* 99 (2015) 69–76.
- [26] F. Granberg, K. Nordlund, M.W. Ullah, K. Jin, C. Lu, H. Bei, L. Wang, F. Djurabekova, W. Weber, Y. Zhang, Mechanism of radiation damage reduction in equiatomic multicomponent single phase alloys, *Phys. Rev. Lett.* 116 (2016) 135504.
- [27] E. Levo, F. Granberg, C. Fridlund, K. Nordlund, F. Djurabekova, Radiation damage buildup and dislocation evolution in Ni and equiatomic multicomponent Ni-based alloys, *J. Nucl. Mater.* 490 (2017) 323–332.
- [28] Y. Zou, H. Ma, R. Spolenak, Ultrastrong ductile and stable high-entropy alloys at small scales, *Nat. Commun.* 6 (2015) 7748.
- [29] N.A.P.K. Kumar, C. Li, K.J. Leonard, H. Bei, S.J. Zinkle, Microstructural stability and mechanical behavior of FeNiMnCr high entropy alloy under ion irradiation, *Acta Mater* 113 (2016) 230–244.
- [30] F. Otto, Y. Yang, H. Bei, E.P. George, Relative effects of enthalpy and entropy on the phase stability of equiatomic high-entropy alloys, *Acta Mater* 61 (2013) 2628–2638.
- [31] C. Lu, K. Jin, L.K. Béland, F. Zhang, T. Yang, Q. Liang, Y. Zhang, H. Bei, H.M. Christen, R.E. Stoller, Direct Observation of Defect Range and Evolution in Ion-Irradiated Single Crystalline Ni and Ni Binary Alloys, *Sci. Rep.* 6 (2016) 19994.
- [32] K. Jin, C. Lu, L.M. Wang, J. Qu, W.J. Weber, Y. Zhang, H. Bei, Effects of compositional complexity on the ion-irradiation induced swelling and hardening in Ni-containing equiatomic alloys, *Scr. Mater.* 119 (2016) 65–70.
- [33] G. Velisa, M.W. Ullah, H. Xue, K. Jin, M.L. Crespiello, H. Bei, W.J. Weber, Y. Zhang, Irradiation-induced damage evolution in concentrated Ni-based alloys, *Acta Mater* 135 (2017) 54–60.
- [34] G. Velisa, E. Wendler, S. Zhao, K. Jin, H. Bei, W.J. Weber, Y. Zhang, Delayed damage accumulation by thermal suppression of defect production in concentrated solid solution alloys, *Mater. Res. Lett.* 6 (2018) 136–141.
- [35] Y. Zhang, G.M. Stocks, J. Ke, C. Lu, H. Bei, B.C. Sales, L. Wang, L.K. Béland, R.E. Stoller, G.D. Samolyuk, Influence of chemical disorder on energy dissipation and defect evolution in concentrated solid solution alloys, *Nat. Commun.* 6 (2015) 8736.
- [36] K. Jin, B.C. Sales, G.M. Stocks, G.D. Samolyuk, M. Daene, W.J. Weber, Y. Zhang, H. Bei, Tailoring the physical properties of Ni-based single-phase equiatomic alloys by modifying the chemical complexity, *Sci. Rep.* 6 (2016) 20159.
- [37] K.Y. Tsai, M.H. Tsai, J.W. Yeh, Sluggish diffusion in Co–Cr–Fe–Mn–Ni high-entropy alloys, *Acta Mater* 61 (2013) 4887–4897.
- [38] H.-S. Do, B.-J. Lee, Origin of radiation resistance in multi-principal element alloys, *Sci. Rep.* 8 (2018) 16015.
- [39] M.W. Ullah, D.S. Aidhy, Y. Zhang, W.J. Weber, Damage accumulation in ion-irradiated Ni-based concentrated solid-solution alloys, *Acta Mater* 109 (2016) 17–22.
- [40] T.D. De La Rubia, M. Guinan, New mechanism of defect production in metals: A molecular-dynamics study of interstitial-dislocation-loop formation in high-energy displacement cascades, *Phys. Rev. Lett.* 66 (1991) 2766.
- [41] M. Kiritani, Story of stacking fault tetrahedra, *Mater. Chem. Phys.* 50 (1997) 133–138.
- [42] S.J. Zinkle, L.E. Seitzman, W.G. Wolfer, Energy calculations for pure metals, *Philos. Mag.* A 55 (1987) 111–125.
- [43] R.B. Sills, N. Bertin, A. Aghaei, W. Cai, Dislocation Networks and the Microstructural Origin of Strain Hardening, *Phys. Rev. Lett.* 121 (2018) 085501.
- [44] T.S. Byun, On the stress dependence of partial dislocation separation and deformation microstructure in austenitic stainless steels, *Acta Mater* 51 (2003) 3063–3071.
- [45] M.-R. He, S. Wang, S. Shi, K. Jin, H. Bei, K. Yasuda, S. Matsumura, K. Higashida, I.M. Robertson, Mechanisms of radiation-induced segregation in Cr-FeCoNi-based single-phase concentrated solid solution alloys, *Acta Mater* 126 (2017) 182–193.
- [46] W.L. Chen, X.Y. Ding, Y.C. Feng, X.J. Liu, K. Liu, Z.P. Lu, D.Z. Li, Y.Y. Li, C.T. Liu, X.Q. Chen, Vacancy formation enthalpies of high-entropy FeCoCrNi alloy via first-principles calculations and possible implications to its superior radiation tolerance, *J. Mater. Sci. Technol.* 34 (2018) 355–364.
- [47] D. Chen, Y. Tong, H. Li, J. Wang, Y.L. Zhao, A. Hu, J.J. Kai, Helium accumulation and bubble formation in FeCoNiCr alloy under high fluence He<sup>+</sup> implantation, *J. Nucl. Mater.* 501 (2018) 208–216.
- [48] K. Nordlund, S.J. Zinkle, A.E. Sand, F. Granberg, R.S. Averback, R.E. Stoller, T. Suzudo, L. Malerba, F. Banhart, W.J. Weber, F. Willaime, S.L. Dudarev, D. Simeone, Primary radiation damage: A review of current understanding and models, *J. Nucl. Mater.* 512 (2018) 450–479.
- [49] S. Plimpton, Fast parallel algorithms for short-range molecular dynamics, *J. Comput. Phys.* 117 (1995) 1–19.
- [50] A. Zaddach, C. Niu, C. Koch, D. Irving, Mechanical properties and stacking fault energies of NiFeCrCoMn high-entropy alloy, *JOM* 65 (2013) 1780–1789.
- [51] Y. Tong, K. Jin, H. Bei, J. Ko, D.C. Pagan, Y. Zhang, F. Zhang, Local lattice distortion in NiCoCr, FeCoNiCr and FeCoNiCrMn concentrated alloys investigated by synchrotron X-ray diffraction, *Mater. Des.* 155 (2018) 1–7.
- [52] F.X. Zhang, Y. Tong, K. Jin, H.B. Bei, W.J. Weber, A. Huq, A. Lanzirrotti, M. Newville, D.C. Pagan, J.Y.P. Ko, Y.W. Zhang, Chemical complexity induced local structural distortion in NiCoFeMnCr high-entropy alloy, *Mater. Res. Lett.* 6 (2018) 450–455.
- [53] S. Nose, Constant-temperature molecular dynamics, *J. Phys. Condens. Matter* 2 (1990) SA115–SA119.
- [54] F. Gao, D. Chen, W. Hu, W.J. Weber, Energy dissipation and defect generation in nanocrystalline silicon carbide, *Phys. Rev. B* 81 (2010) 184101.
- [55] W.M. Choi, Y. Kim, D. Seol, B.J. Lee, Modified embedded-atom method interatomic potentials for the Co–Cr, Co–Fe, Co–Mn, Cr–Mn and Mn–Ni binary systems, *Comput. Mater. Sci.* 130 (2017) 121–129.
- [56] W.-M. Choi, Y.H. Jo, S.S. Sohn, S. Lee, B.-J. Lee, Understanding the physical metallurgy of the CoCrFeMnNi high-entropy alloy: an atomistic simulation study, *npj Comput. Mater* 4 (2018) 1–9.
- [57] Y. Li, R. Li, Q. Peng, Enhanced surface bombardment resistance of the CoNiCr-FeMn high entropy alloy under extreme irradiation flux, *Nanotechnol* 31 (2019) 025703.
- [58] J.F. Ziegler, J.P. Biersack, The stopping and range of ions in matter, in: *Treatise on Heavy-Ion Science*, Springer, 1985, pp. 93–129.
- [59] A. Stukowski, Structure identification methods for atomistic simulations of crystalline materials, *Model. Simul. Mater. Sci. Eng.* 20 (2012) 45021.
- [60] K. Nordlund, M. Ghaly, R.S. Averback, M. Caturia, D.T. Rubia, J. Tarus, Defect production in collision cascades in elemental semiconductors and FCC metals, *Phys. Rev. B Condens. Matter.* 57 (1998) 7556–7570.
- [61] A. Stukowski, V.V. Bulatov, A. Arsenlis, Automated identification and indexing of dislocations in crystal interfaces, *Model. Simul. Mater. Sci. Eng.* 20 (2012) 085007.
- [62] J.D. Honeycutt, H.C. Andersen, Molecular dynamics study of melting and freezing of small Lennard-Jones clusters, *J. Phys. Chem.* 91 (1987) 4950–4963.
- [63] D. Faken, H. Jönsson, Systematic analysis of local atomic structure combined with 3D computer graphics, *Comput. Mater. Sci.* 2 (1994) 279–286.
- [64] F.R. Nabarro, *Theory of Crystal Dislocations*, Oxford: Clarendon Press, New York, 1967.
- [65] L.K. Béland, C. Lu, Y.N. Osetskiy, G.D. Samolyuk, A. Caro, L. Wang, R.E. Stoller, Features of primary damage by high energy displacement cascades in concentrated Ni-based alloys, *J. Appl. Phys.* 119 (2016) 085901.
- [66] Y. Mishin, Atomistic modeling of the  $\gamma$  and  $\gamma'$ -phases of the Ni–Al system, *Acta Mater* 52 (2004) 1451–1467.
- [67] W. Setyawan, G. Nandipati, K.J. Roche, H.L. Heinisch, B.D. Wirth, R.J. Kurtz, Displacement cascades and defects annealing in tungsten, Part I: Defect database from molecular dynamics simulations, *J. Nucl. Mater.* 462 (2015) 329–337.
- [68] Z. Zhang, M.M. Mao, J. Wang, B. Gludovatz, Z. Zhang, S.X. Mao, E.P. George,

- Q. Yu, R.O. Ritchie, Nanoscale origins of the damage tolerance of the high-entropy alloy CrMnFeCoNi, *Nat. Commun.* 6 (2015) 10143.
- [69] Q. Ding, Y. Zhang, X. Chen, X. Fu, D. Chen, S. Chen, L. Gu, F. Wei, H. Bei, Y. Gao, Tuning element distribution, structure and properties by composition in high-entropy alloys, *Nature* 574 (2019) 223–227.
- [70] X.-X. Wang, L.-L. Niu, S. Wang, Energetics analysis of interstitial loops in single-phase concentrated solid-solution alloys, *J. Nucl. Mater.* 501 (2018) 94–103.
- [71] I. Neklyudov, V. Voyevodin, Features of structure-phase transformations and segregation processes under irradiation of austenitic and ferritic-martensitic steels, *J. Nucl. Mater.* 212 (1994) 39–44.
- [72] C. Lu, T.-N. Yang, K. Jin, G. Velisa, P. Xiu, Q. Peng, F. Gao, Y. Zhang, H. Bei, W.J. Weber, Irradiation effects of medium-entropy alloy NiCoCr with and without pre-indentation, *J. Nucl. Mater.* 524 (2019) 60–66.
- [73] G.S. Was, *Fundamentals of Radiation Materials Science: Metals and Alloys*, Second ed., SpringerNature, Springer-Verlag GmbH Berlin Heidelberg, 2016.
- [74] D.J. Bacon, T.D. Rubia, Molecular dynamics computer simulations of displacement cascades in metals, *J. Nucl. Mater.* 216 (1994) 275–290.
- [75] D. Chen, F. Gao, W. Hu, S.Y. Hu, D. Terentyev, X. Sun, H.L. Heinisch, C.H. Henager, M.A. Khaleel, Migration of Cr-vacancy clusters and interstitial Cr in  $\alpha$ -Fe using the dimer method, *Phys. Rev. B* 81 (2010) 064101.
- [76] S. Zhao, Y. Osetsky, A.V. Barashev, Y. Zhang, Frenkel defect recombination in Ni and Ni-containing concentrated solid-solution alloys, *Acta Mater* 173 (2019) 184–194.
- [77] S. Zhao, G.M. Stocks, Y. Zhang, Defect energetics of concentrated solid-solution alloys from ab initio calculations: Ni 0.5 Co 0.5, Ni 0.5 Fe 0.5, Ni 0.8 Fe 0.2 and Ni 0.8 Cr 0.2, *Phys. Chem. Chem. Phys.* 18 (2016) 24043–24056.
- [78] J. Tucker, T. Allen, D. Morgan, Ab initio defect properties for modeling radiation-induced segregation in Fe–Ni–Cr alloys, in: *Proceedings of the International Symposium Environmental Degradation of Materials in Nuclear Power Systems*, 13th ed, Whistler, BC, Can, 2007, pp. 1004–1014.
- [79] L. Delczeg, E. Delczeg-Czirjak, B. Johansson, L. Vitos, Assessing common density functional approximations for the ab initio description of monovacancies in metals, *Phys. Rev. B* 80 (2009) 205121.
- [80] W. Wycisk, M. Feller-Kniepmeier, Quenching experiments on high-purity nickel, *Phys. Status Solidi A* 37 (1976) 183–191.
- [81] L. Smedskjaer, M. Fluss, D. Legnini, M. Chason, R. Siegel, The vacancy formation enthalpy in Ni determined by positron annihilation, *J. Phys. F: Met. Phys.* 11 (1981) 2221.